Lab on a Chip

PAPER

View Article Online
View Journal | View Issue

Cite this: *Lab Chip*, 2026, **26**, 3069

Stretchable mesoporous electrodes as a versatile platform for minimally invasive surgical devices

Michael Abraham Listyawan,[a] Chi Cong Nguyen,[a] Tran Bach Dang,[a] Nhat Mihn Doan,[a] Quang Anh Nguyen,[a] Yulin Qiu,[ab] Eva Tomaskovic-Crook,[def] Mostafa Kamal Masud,[c] Yusuke Yamauchi,[c] Jeremy Micah Crook,[def] Mohit Naresh Shivdasani,[bg] Thanh Nho Do[bg] and Hoang-Phuong Phan *[ag]

Received 6th February 2026,
Accepted 8th April 2026

DOI: 10.1039/d6lc00110f

rsc.li/loc

Minimally invasive surgery (MIS) is a vital procedure for the treatment of several cardiac and neural diseases, such as clearing clogged arteries, pacing irregular heartbeats, monitoring intracranial pressure, and draining excess cerebrospinal fluid from the brain. Recent research advances in soft electronics demonstrate the potential of integrated electrodes in enhancing MIS performance, enabling *in situ* biopotential measurement, electrical stimulation, and bioimpedance sensing. The addition of these modalities expands the potential of MIS to deliver targeted cardiac interventions or further minimize risks through brain activity monitoring during the procedure. Existing sensor-integrated catheters still exhibit several drawbacks, such as a sizable increase in catheter profile, inconsistent electrode performance, limited fabrication scalability, and a lack of active steering capability. We report here the development of flexible electrodes using mesoporous gold as a functional layer with enhanced surface impedance characteristics for recording, high charge injection capacity for stimulation, and mechanical compliance for integration into a wide range of MIS tools with varied diameters. Integrating the electrode into a soft robotic catheter driven by an embedded microfluidic channel and microtubing demonstrates a manoeuvrable system with electrical and mechanical stability under various bending conditions, together with a low system profile suitable for a minimally invasive procedure. Through a set of *ex vivo* and *in vitro* experiments, we demonstrate the potential of our system for various biomedical applications, including field potential measurement, bioimpedance sensing, and cardiac pacing, that can leverage the capability of MIS procedures.

1. Introduction

Minimally invasive surgery (MIS) has dramatically transformed both cardiology and neurology, delivering more precise and safer interventions than conventional open procedures. Among these, catheterization is a core procedure, offering access to deep anatomical structures while minimizing tissue trauma, incision-related risks, and infection. In neurosurgery, external ventricular drainage (EVD) catheters are routinely employed to monitor intracranial pressure[1–4] and relieve hydrocephalus, highlighting their diagnostic and therapeutic utility. In cardiology, catheterization underpins both ablation therapies[5] and temporary transvenous cardiac pacing,[6–9] enabling targeted arrhythmia treatment[10,11] and emergency rhythm stabilization. These well-established applications highlight the clinical efficacy of catheters and the potential for broadening their functionality to enhance MIS outcomes.

Embedding multi-modal sensing capabilities onto catheters is expected to elevate MIS performance by enabling more precise and responsive interventions. Recent advances include fibre-optic sensors integrated into catheter tips to monitor pressure,[12] temperature,[13–15] force,[16,17] and molecular composition in real time,[18,19] greatly enriching intraoperative feedback. In neurosurgery, prototype flexible EVD catheters capable of recording local field potentials (LFPs) during placement can potentially reduce postoperative brain trauma by

[a] *School of Mechanical and Manufacturing Engineering, The University of New South Wales, Sydney, NSW 2052, Australia. E-mail: hp.phan@unsw.edu.au*
[b] *School of Biomedical Engineering, The University of New South Wales, Sydney, NSW 2052, Australia*
[c] *Australian Institute of Bioengineering and Nanotechnology (AIBN) and School of Chemical Engineering, The University of Queensland, St Lucia, QLD 4072, Australia*
[d] *Arto Hardy Family Biomedical Innovation Hub, Chris O'Brien Lifehouse, Camperdown, NSW, 2050 Australia*
[e] *School of Medical Sciences, Faculty of Medicine and Health, The University of Sydney, Camperdown, NSW, 2006 Australia*
[f] *Intelligent Polymer Research Institute and Australian Institute of Innovative Materials, Innovation Campus, University of Wollongong, Squires Way, Fairy Meadow, NSW, 2519 Australia*
[g] *Tyree Foundation Institute of Health Engineering, University of New South Wales, Sydney, NSW 2052, Australia*

offering direct electrophysiological guidance during insertion.[20] In electrophysiological cardiology, impedance-based sensing at the catheter–tissue interface has emerged as a powerful tool to assess contact quality, detect dysfunctional tissues, and provide feedback to ensure a stable interface between devices and tissues. Additionally, embedding cardiac pacing functionality can potentially open new therapeutic interventions combined with sensing capabilities. Collectively, these innovations emphasize the need for embedding real-time, multi-parametric sensing and added functionality into catheters to enhance procedural safety, diagnostic precision, and therapeutic efficacy.

The development of electrode-integrated catheters centres on two critical requirements, mechanical compliance and electrochemical characteristics. Recent advances in integrated flexible electrodes demonstrate soft, conformable electrodes capable of achieving spatial cardiac mapping while conforming to the dynamic contours of organs.[21–23] Incorporating soft, stretchable designs is a common method to improve the mechanical properties of electrodes, enabling them to accommodate the bending and deformation of catheters and broadening their applicability for integration into large-deformation catheter systems or soft robots. Examples of this approach include the development of a 3D buckled structure to enhance mechanical stretchability while allowing multimodal sensing. However, the out-of-plane configuration increases the device thickness, limiting the applications of 3D buckled structures mainly to scale systems such as balloon catheters.[24] Besides mechanical designs, advanced material selections and functionalization of nanomaterials have also been explored to enhance the electrochemical characteristics of the electrode. The use of conductive polymers such as PEDOT: PSS as a coating can lower the impedance of a typical metallic electrode with softer mechanical properties suitable for tissue compliance.[25–28] Despite their intrinsic mechanical flexibility and low impedance, these materials exhibit several limitations, such as their compatibility with standard lithography processes and their biostability and reliability, especially for polymers whose quality may vary depending on synthesis processes. Other inorganic nanocoating materials, such as Pt black and iridium oxide (IrO_x), also offer a significantly lower impedance and high charge storage capacity; however, IrO_x coating is intrinsically brittle[29] and thick Pt-black coating has a thicker profile that might affect the structural integrity of flexible electrodes.[30] Another approach employs metal electrodes laser cut into a serpentine shape and hot-pressed by sandpaper to enhance surface roughness, thereby reducing electrochemical impedance. However, this fabrication approach is difficult to scale and only offers minimal impedance enhancement.[20,31] It is noteworthy that most published research focuses on embedding electrodes onto passive catheters, while the integration of functional devices onto active and highly steerable systems, such as soft robotics, is relatively unexplored. Specifically, emerging soft robotic platforms that utilize microfluidic or hydraulic actuation could greatly benefit from integrated electrodes to broaden their use cases. However, such integration introduces additional constraints related to interfacial adhesion and long-term electrochemical stability under repeated manoeuvres. The development of a scalable process and high-performance electrodes, together with their integration into controllable catheter systems, therefore, presents promising potential for enhancing the capabilities of MIS.

This paper presents a flexible, stretchable, low-impedance electrode integrated into a soft robotic catheter for multimodal sensing and stimulation by combining rapid prototyping techniques, including direct laser machining and low-temperature electrochemical deposition. The design incorporates (i) serpentine geometries that enhance mechanical compliance for the highly deformable soft catheters, and (ii) a mesoporous network that reduces the electrochemical impedance spectra (EIS) by one order of magnitude compared to conventional flat electrodes. The mesoporous architecture substantially increased the charge injection capacity compared to flat electrodes by tenfold, enabling a higher permitted charge delivery for broader therapeutic and diagnostic applications. Benchtop characterization of the flexible electrode confirms its high performance in impedance sensing, cardiac pacing, along with a low mechanical profile that minimizes invasiveness during catheterization procedures and supports smooth robotic manoeuvrability.

2. Experimental section

2.1. Flexible serpentine electrode fabrication

A commercial PI layer [3-1966-01, ASOne] with a thickness of 12.5 μm is attached to a Si substrate using Kapton tape. Metal film deposition *via* an E-beam evaporation PVD system [Lesker PVD75, Kurt. J. Lesker Company] forms Ti/Au films with a thickness of 20 nm and 200 nm, respectively. Another PI layer is then spin-coated on top of the gold deposited film at 2000 rpm for 30s, followed by soft bake at 110 °C for 1 minute, serving as an encapsulation layer. Subsequently, a positive photoresist layer [ECI3012, MicroChemicals GmbH] is spin-coated at 4000 rpm for 30s and soft-baked at 110 °C for 1 minute. The photoresist layer is then exposed using direct write lithography with the exposure levels of 100 J/m2 [MicroWriter ML3 Pro, Durham Magneto Optics]. Afterwards, the film is developed in a TMAH-based developer [AZ2026, MicroChemcials GmbH] to create electrode openings on the PI encapsulation layer. The Au/PI film with an encapsulation layer is then aligned with a UV laser pattern (class 1 Samurai Marking System, DPSS Lasers with the smallest resolution of 7 μm) to cut through serpentine-shaped electrodes with the following operational parameters, 0.5% of output, 105 kHz laser power, 1100 mm s^{-1} laser speed, and 8 cycles after focus is adjusted accordingly.

2.2. Electrochemical deposition of mesoporous Au

The mesoporous gold layer was fabricated through an electrochemical deposition process using a combination of self-

assembling block copolymeric micelles, PS-b-PEO (polystyrene-block-polyethylene glycol), and gold precursors, as an electrolyte. To create the micelle solution, 10 mg of PS(18 k)-b-PEO(7.5 k) was dissolved by continuous stirring in 3 ml of THF (Tetrahydrofuran) [99.9%, Sigma-Aldrich]. Afterwards, 1.5 ml of pure ethanol [99.5%, Sigma-Aldrich] was added to the solution. Subsequently, 1 ml of 40 mM $HAuCl_4$ diluted in deionized water (DI-water) is added as Au precursor. Lastly, adding 2.5 ml of DI water completes the Au electrolyte with micelle for the subsequent deposition process. The electrochemical deposition was conducted in a single reaction cell using a three-electrode configuration with Pt (012961, ALS) and Ag/AgCl (RE1-S, ALS) as the counter and reference electrodes, respectively. The flexible flat gold electrode (*i.e.*, the working electrode) was submerged in the micelle solution, and chronoamperometry was conducted by applying −0.5 V for 1000s. After electrochemical deposition, the mesoporous electrode underwent solvent wash using THF at 40 °C.

2.3. Mesostructure and electrochemical characterization

Material morphology was observed using field-emission scanning electron microscopy (FE-SEM) [Nova NanoSEM 450, FEI] operated at 10 kV accelerating voltage. The pore size was measured by analysing the SEM pictures through image processing software. Electrochemical measurements were conducted using a potentiostat [PalmSens4, PalmSens]. For cyclic voltammetry (CV) and electrochemical impedance spectroscopy (EIS) measurements, a three-electrode setup was utilized where Ag/AgCl (RE1-S, ALS) and Pt (012961, ALS) served as the reference and counter electrode, respectively. The working electrode was the target electrode which can be a non-mesoporous gold or a mesoporous gold electrode. CV was performed by submerging the electrodes in 0.5 M H_2SO_4 at various scan rates, while EIS was performed under the solution of 1× PBS diluted in DI water.

Charge injection capacity was characterized by using a common 3-electrode setup. A customized circular shape electrode with a diameter of 500 μm is utilized for this experiment. The biphasic stimulation was administered by using a biphasic stimulator [4CH Neurostimulator, Zudabyte Labs]. Stimulation was applied between the working and counter electrodes. The voltage transient was measured using an isolated oscilloscope [125B Series Industrial Scopemeter, Fluke]. Charge injection capacity was determined using cathodic biphasic pulses with a phase duration of 1000 μs and defined as the maximum injectable charge that resulted in a polarisation of the electrode up to the cathodic water window limit (determined through cyclic voltammetry). For *ex vivo* impedance sensing demonstration, radio frequency ablation was generated by a commercially available electrocautery unit [Surtron 120, LED] with a maximum applied power of 120 W. The impedance level of the tissue was measured before and after ablation, with a frequency range from 1 Hz to 100 kHz, using a portable potentiostat [Palmsens4, Palmsens].

2.4. Mechanical flexibility

The mechanical stability was characterized using a linear stage [LSM Series, Zaber] modified with a customized 3D printed clamp specifically designed for the stability test. The catheter was clamped at both ends and displaced incrementally from 1 mm to 10 mm. The impedance of the electrode was measured after each bending cycle, to validate its performance stability.

2.5. Catheter invasiveness characterization

We utilized a 0.6% agarose gel synthesized with an established procedure to mimic the mechanical stiffness of the brain model.[32] The invasiveness characteristics were conducted by recording video with a digital microscope [AM7515, Dino-lite] during insertion and ejection procedures to capture the crack formed in the surface of the brain model. Image processing was then applied to analyse the dimension of the crack and benchmark that with and without the electrode. Additionally, a universal testing machine [Series F, Mark-10] was used for detecting the average insertion force and characterizing the recommended insertion method of the integrated catheter.

2.6. Benchtop characterization of mesoporous electrode signal recording

The typical electrode setup consisted of Pt electrodes and an Ag/AgCl electrode connected to a function generator [72-3555, TENMA] to induce a controlled electrical field. The flexible electrode was connected to an oscilloscope with a bandwidth up to 50 MHz and a sampling rate of 1 GS/s [TBS1000C-AU, Tektronix] for potential reading. With all electrodes submerged in a 1× PBS solution, a sine wave electrical field with frequency variations is applied, and the recording is made through the oscilloscope.

2.7. *In vitro* human cardiac organoid pacing demonstration setup and analysis

Cardiac organoids were generated from embryoid bodies (EBs) derived from human pluripotent stem cell (hPSC) line JMC1i-SS9 (in-house derived, mycoplasma negative and approved for use by the University of Wollongong Human Research Ethics Committee HE14/049).[33,34] Briefly, hPSCs were dissociated, resuspended in mTeSR™ Plus plating medium supplemented with ROCK inhibitor (Stem Cell Technologies), and seeded into 96-well, round-bottomed, ultra-low attachment plates (Corning) to form EBs. EBs were then differentiated by staged Wnt signalling modulation, involving initial induction of cardiac mesoderm (2 days), definitive cardiac cell lineages (2 days), followed by epicardial organ formation (2 days), and induction of blood vessel formation (2 days). Finally, from day 9, organoids were maintained in maturation medium, comprising RAPMI 1640 and B-27 supplement, with medium changes performed every other day until required for further experimentation.

The pacing demonstration setup was conducted in a customized, 3D-printed fixture that formed a cone-shaped chamber. The stimulation was administered through the mesoporous gold electrode connected to a multifunctional test and measurement device [Analog Discovery 3, Digilent] while being recorded using Digital Microscope Dinocam [AM7515, Dino-lite] to monitor cardiac organoid beating.

3. Results and discussion

3.1. Design and fabrication of stretchable mesoporous electrodes

Fig. 1a shows the proposed serpentine-shaped flexible, stretchable electrodes, which are functionalized with a nanothin mesoporous gold layer and conformally integrated onto the tubular bodies of catheters and soft robotic systems. The serpentine geometry incorporates two rectangular terminals that simplify handling and assembly of electrodes of various dimensions onto curvilinear surfaces. As illustrated in Fig. 1b, these electrodes offer multiple sensing and actuation modalities such as signal recording, bioimpedance monitoring, and cardiac pacing. For instance, an external ventricular drainage (EVD) catheter can leverage LFP measurements for continuous assessment of brain activity, enabling surgeons to optimally mitigate post-surgical traumas.[20] MISs equipped with these electrodes provide temporary cardiac pacing to modulate blood flow and pressure during endovascular procedures.

To achieve a mechanically compliant electrode with significantly reduced impedance, we employed a hybrid fabrication approach that combines top-down and bottom-up

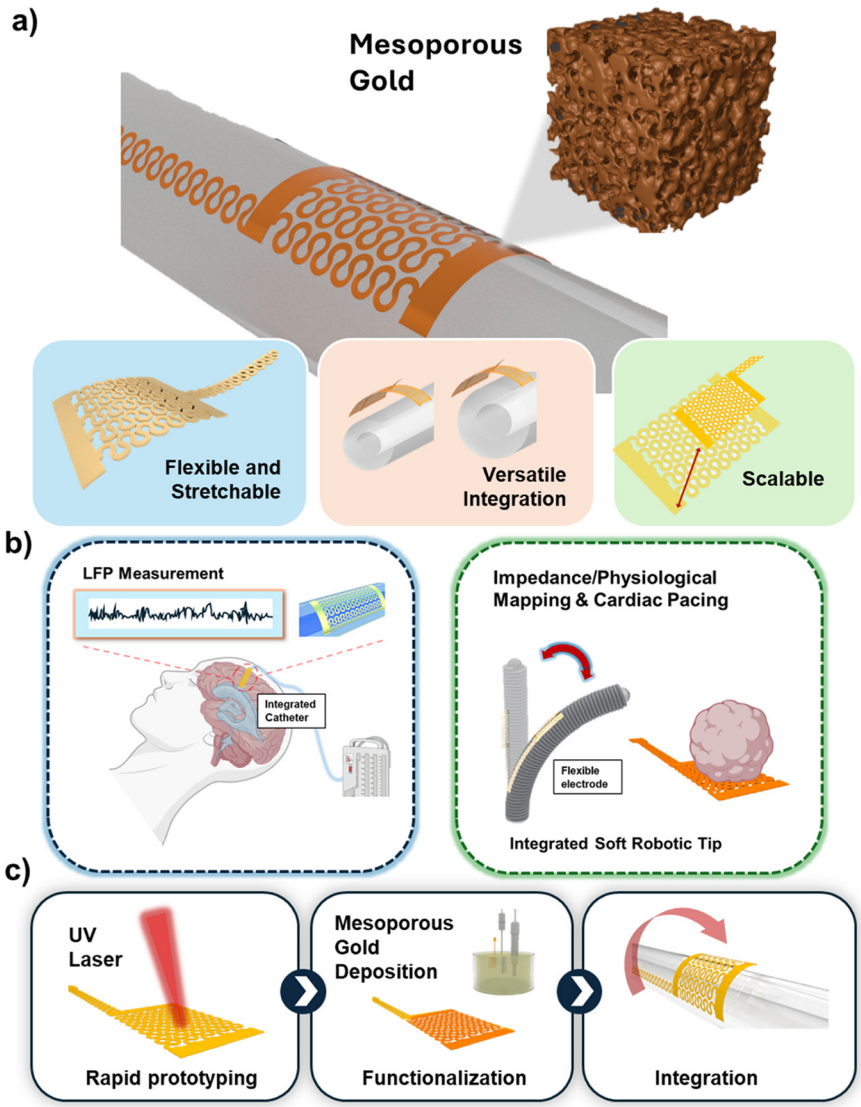

Fig. 1 Overview of flexible mesoporous gold electrode for integration with MIS tools. (a) Schematic of an integrated flexible electrode showcasing its advantages and the mesoporous gold layer. (b) Its potential application for LFP measurement, impedance/physiological mapping, and cardiac pacing. (c) The fabrication and integration methods of the flexible electrode, including rapid prototyping using laser, electrodeposition of mesoporous gold, and integration on a catheter, as common MIS tools.

techniques (Fig. 1c). The fabrication process began with thermal evaporation of a Ti/Au (10 nm/100 nm) layer onto a polyimide film attached to a Si substrate, followed by spin-coating another PI layer that serves as an encapsulation layer. Photolithography and wet etching defined openings for electrode sites and contact pads. Subsequently, UV-laser machining yielded the serpentine layouts with high design flexibility and rapid patterning throughput. The serpentine structure is selected due to its proven ability to improve flexibility and stretchability, which aligns with our application needs of integration to various MIS platforms.[35,36] Electrochemical deposition through the exposed windows forms an ultrathin mesoporous gold layer that substantially enhances the electrochemical performance (Fig. S1). The completed serpentine electrodes were then released from the silicon carrier using a water-soluble tape and transferred onto a catheter or a soft robotic surface *via* an adhesive layer [sil-poxy, smooth-on]. Details of the fabrication method for the soft robot platform can be found elsewhere.[37]

3.2. Material synthesis of mesoporous gold

To create mesoporous architectures, we utilized electrochemical deposition from an aqueous solution containing amphiphilic block copolymer micelles and gold precursors.[38,39] The hydrophobic micelle cores serve as sacrificial templates for the nanopores, while the hydrophilic domains coordinate with gold ions to form a micelle-gold complex, as illustrated in Fig. 2a and b. During deposition, a constant potential is applied under chronoamperometry control to track the redox reaction at the electrode interface (Fig. 2c). The positively charged micelles migrate toward the working electrode, where the ions are reduced to metallic gold.[40,41] The micelles remain embedded within the growing film, thereby forming an interconnected mesoporous network. Afterwards, the remaining micelles are removed through proper solvent wash. The overall growth process of mesoporous gold is visualized in the SI (Fig. S2). A gradual increase in resistance during mesoporous film growth, resulting in a steady reduction of current during the deposition period, correlates with the progressive thickening of the deposited layer. Our previous studies explored and optimized the deposition conditions required to form mesoporous gold films with various pore sizes. Extensive materials characterization, including transmission electron microscopy (TEM) imaging, pore size distribution, gold micelle synthesis optimization, and uniformity analysis, has been reported in those publications. However, it should be noted that the previous studies were conducted on conventional rigid substrates such as Si and glass, and mesoporous gold growth is highly substrate dependent. For flexible substrates such as polyimide, the growth of mesoporous structures may induce variations in their pore sizes and morphology. Utilizing the previously optimized parameters as a benchmark, we fabricated mesoporous gold films on a soft substrate at a variety of working potentials and deposition durations.

The resulting porous structure significantly increased the effective surface area and reduced electrode impedance as verified by electrochemical impedance spectroscopy (EIS) in 1× phosphate-buffered saline (PBS) (Fig. 2d). Impedance values averaged across samples demonstrate a reduction of at least an order of magnitude at 1 kHz compared to planar Au. Scanning electron microscopy (SEM) images with different magnifications (Fig. 2e) enabled quantitative pore size analysis *via* established image processing methods.[42] Using a fixed block-copolymer, the pore dimensions can be tuned by varying the deposition potential between −0.3 V and −0.7 V (Fig. S3 and S4). Qualitatively, SEM images of the mesoporous gold grown on a soft substrate have comparable morphologies when compared to the mesoporous gold grown on a rigid Si substrate.[42] Quantitatively, there were pore size variances that ranged from 17 nm to 36 nm on average as the voltage levels decreased to −0.7 V which was still in range compared to the pore size distribution of mesoporous gold grown in a rigid Si substrate. At this voltage level, rapid reduction reaction disrupts micelle integrity, whereas potentials below −0.7 V preserve micelle quality throughout the deposition process. EIS characterization across these conditions reveals only a minor impedance difference arising from pore-size variation (Fig. S5). This suggests that the active surface area of mesoporous gold only slightly changes regardless of the pore size differences. However, continual mesoporous gold deposition at −0.7 V levels is not sustainable as it affects the gold micelle solution by changing the colour after several electrochemical deposition processes. Based on the micelle solution quality, −0.5 V was selected as the optimal deposition potential. For EIS and Impedance characterization, A common circular shape gold on polyimide electrode was utilized with a diameter of 1 mm. We further examined the influence of deposition time on the microstructure formation (Fig. S6). Uniform mesoporous films are achieved at 1000s, while extended deposition times to 1500s and 2000s produce gold agglomeration with cauliflower-like morphologies. Although such features may slightly improve the electrochemical properties, they compromise structural uniformity and reproducibility. As a result, we defined −0.5 V and 1000s deposition time as the optimal electrochemical growth conditions for forming high-quality mesoporous Au on stretchable electrodes.

Cyclic voltammetry (CV) further confirmed the enhanced electrochemical properties of mesoporous electrodes. The CV measurements were conducted in a 0.5 M H_2SO_4 solution to maintain surface cleanliness for comparing flat Au and mAu. As shown in Fig. 2f, the mesoporous electrodes exhibited distinct differences in redox peaks, particularly between 0.8 and 1.5 V, corresponding to the adsorption and desorption of oxygen with respect to the Ag/AgCl reference. A noticeable increase in the reduction peak at 0.9 V reflected an improved electron transfer kinetics enabled by the porous structures. Integrating the reduction current revealed an electrochemically active surface area (ECSA) of 2.92 cm^2 for mAu, approximately 6 times larger than flat Au (0.54 cm^2), providing substantially more reduction sites. The charge storage capacity also significantly increased

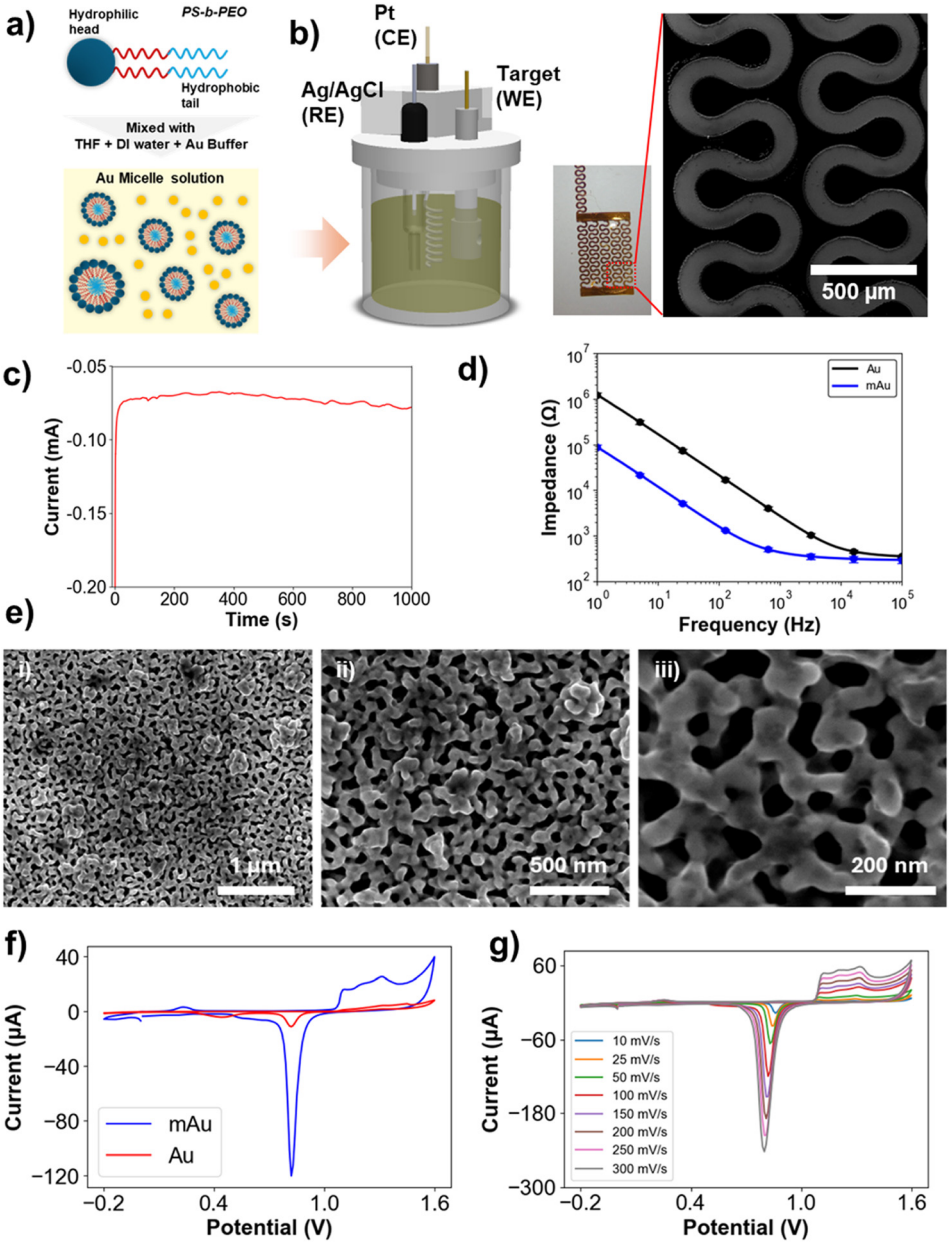

Fig. 2 (a) Conceptual visualization of mesoporous gold electrochemical deposition using micelle gold solution as a template. (b) The 3-electrode setup visualization consists of a Pt (CE), Ag/AgCl (RE), and the target electrode (WE), along with a low-magnification SEM image of the flexible electrode post-deposition. (c) Chronoamperometry results during electrochemical deposition of mesoporous gold under −0.5 V for 1000s. (d) EIS results comparison between mesoporous gold (mAu) and flat gold (Au) electrodes. (e) SEM images of mesoporous gold showing the porosity of the layer with (i) low, (ii) medium, and (iii) high magnification. (f) Cyclic voltammetry (CV) results comparison between mesoporous gold (mAu) and flat gold (Au) electrodes in 0.5 M H_2SO_4. (g) CV results of mAu electrodes scan at different rates.

from 0.25 mC cm^2 for flat Au to 1.45 mC cm^2 for mAu, suggesting a greater ability to inject charge safely during electrical stimulation. CV measurement across varied scan rates (Fig. 2g) showed a proportional relationship between peak current and scan rate, indicating that the charge transfer was dominated by a capacitive process rather than redox species. This behaviour confirmed that the electrode response was governed by double-layer capacitance, consistent with the high surface area afforded by the mesoporous architecture.

3.3. Integrated flexible electrode mechanical stability

Smart mechanical designs enable mesoporous electrodes to accommodate the large deformation required for catheterization and soft robotics maneuvers. For specific catheter configurations, flexibility is the primary mechanical characteristic requirement; however, to broaden the applicability of the platform, stretchability characteristic is also essential, especially for soft robotics systems that undergo large

bending angle maneuvers. Therefore, a serpentine structure was intentionally selected as it improves the flexibility and stretchability of the film by minimizing strain induced into mesoporous electrodes. We compared the sample structure through a simple FEA simulation of a 1.4 mm gage length model with linear, kirigami, and serpentine structures. As the model is subjected to the same displacement of 1.4 mm, we can observe that stress concentration occurs along the linear connection. The kirigami structure distributes stress more evenly; however, it forms a high concentration on its edges that might result in cracks and ruptured connections. While serpentine shows the best stress distribution, with the stress concentrated along the outer curves. Through this comparison, we can observe that the stress that the serpentine structure generates with the same displacement applied was significantly lower than that of other structures. Previous studies on similar electrode platforms also utilize serpentine structures to ensure seamless integration with the catheter and have shown stable performance after cycles of bending.[43,44] Finite element analysis (FEA) was used to evaluate the mechanical response and the structural integrity of the flexible serpentine electrode design with a dimension of 3 mm in width and 3.6 mm in length (Fig. S8). FEA was conducted using the commercial software ANSYS 2024 R2. The structure consisted of a 12.5 μm PI substrate and a 200 nm gold layer modelled as a homogeneous thin shell. The catheter was modelled as a tubular shape with a diameter of 2.8 mm, comparable to the typical EVD catheter dimensions. The thin layer is then stretched to fit the condition during electrode integration to a catheter. Each model block was then assigned to its respective material properties assumptions, which are silicone as the tube, PI for the first layer of the electrode, and gold as its second layer, material properties details can be seen in Table S1. Ideal bonding conditions were assumed between all components to compute stress–strain distribution on the electrode surface. Incremental uniaxial forces from 5 N to 50 N were applied at one end of the catheter while the other end of the catheter was fixed (Fig. 3a). Then, we extract the user-defined results on the mechanical response of equivalent elastic strain and equivalent stress. The stress distribution obtained from FEA showed an average stress of 0.19 MPa in the Au layer with a maximum of 2.8 MPa (Fig. 3b). These results were far below the yield strength of Au (approximately 371 MPa), indicating that the device operates safely within the elastic regime.[45] Stress localized primarily within the serpentine traces, demonstrating the ability of the geometry to redistribute axial stretch into bending and rotation along the curved segments. Moreover, the strain analysis similarly revealed a well-distributed deformation profile across the flexible electrode. Under the highest applied load, the average strain was approximately 0.0016% with a maximum strain of 0.012%. The maximum strain appeared on the non-serpentine region near the rectangular areas, influenced by the fixed boundary condition. The overall strain remained well below the fracture limits of thin film gold (approximately 1–3%)[45] and far below the tolerable strain of PI,[46] confirming the robustness of the design for dynamic and conformal deployment.

Additionally, we performed bending simulations to replicate the typical steering motions of soft robotics and catheters, with results summarized in Fig. S9. Both the average and maximum stress and strain values under bending were higher compared to the uniaxial loading (Fig. S10). However, the strain levels remained well below the yield points of both PI and thin film gold. The maximum stress distribution reached 158 MPa, which is higher than the yield strength of PI, which is approximately 81 MPa, and approached the range where localized plastic deformation of the PI layer could occur. Based on these results, the structure might generate a stress concentration that might be affecting the PI substrate after repeated bending cycles. Nevertheless, the serpentine design accommodates bending without significantly compromising the structural integrity of the gold layer, although plasticity in the PI substrate may occur under extreme bending.

Fig. 3(c) and (d) illustrates the experimental setup used to validate the FEA analysis, where electrodes of identical dimensions were integrated onto tubular substrates, resembling common geometries of MIS tools, particularly catheter-based devices.[47,48] The mechanical compliance of the serpentine design allowed for a seamless integration with tubular shapes of varying diameters from 2 mm to 5 mm (Fig. S11). Mechanical characterization of the integrated catheter involved the use of a uniaxial linear stage with customized 3D-printed clamps to apply controlled deflections (Fig. 3e). With both ends of the catheter fixed, uniaxial displacement ranging from 1 mm to 10 mm produced a bending angle exceeding 90 degrees, with electrode impedance measured after each cycle. The results showed slight variation, confirming relatively stable electrical performance under repeated deformation. The electrode integration is well intact after bending cycles, with no noticeable cracks or delamination of mesoporous gold structures from the gold film. Additionally, mesoporous gold morphology was also observed through SEM observation before and after applying bending cycles. SEM images of mesoporous morphology before and after 100 bending cycles are shown (Fig. S12). The mesoporous gold morphologies were not significantly affected. Through image analysis, the pore size remains the same, which is around 27 ± 8 nm. There are some slight changes in the pore size distribution as the total count of larger pore sizes increases after bending.

To further assess robustness under realistic actuation, the flexible electrodes were integrated onto soft, endoscope-like hydraulic robots (2 mm in diameter) constructed from medical heat shrink microtubing, a metallic spring, and a silicone tube forming embedded microfluidic channels. Controlled hydraulic pressure through the microfluidic channels *via* a syringe enables bending of the soft robot up to 90 degrees, simulating complex navigation scenarios. Even after 100 cycles of 90-degree bending, the impedance of the integrated electrode remains unchanged, confirming that the flexible, mesoporous electrodes retained both mechanical integrity and electrochemical functionality under conditions representative of minimally invasive procedures. This result

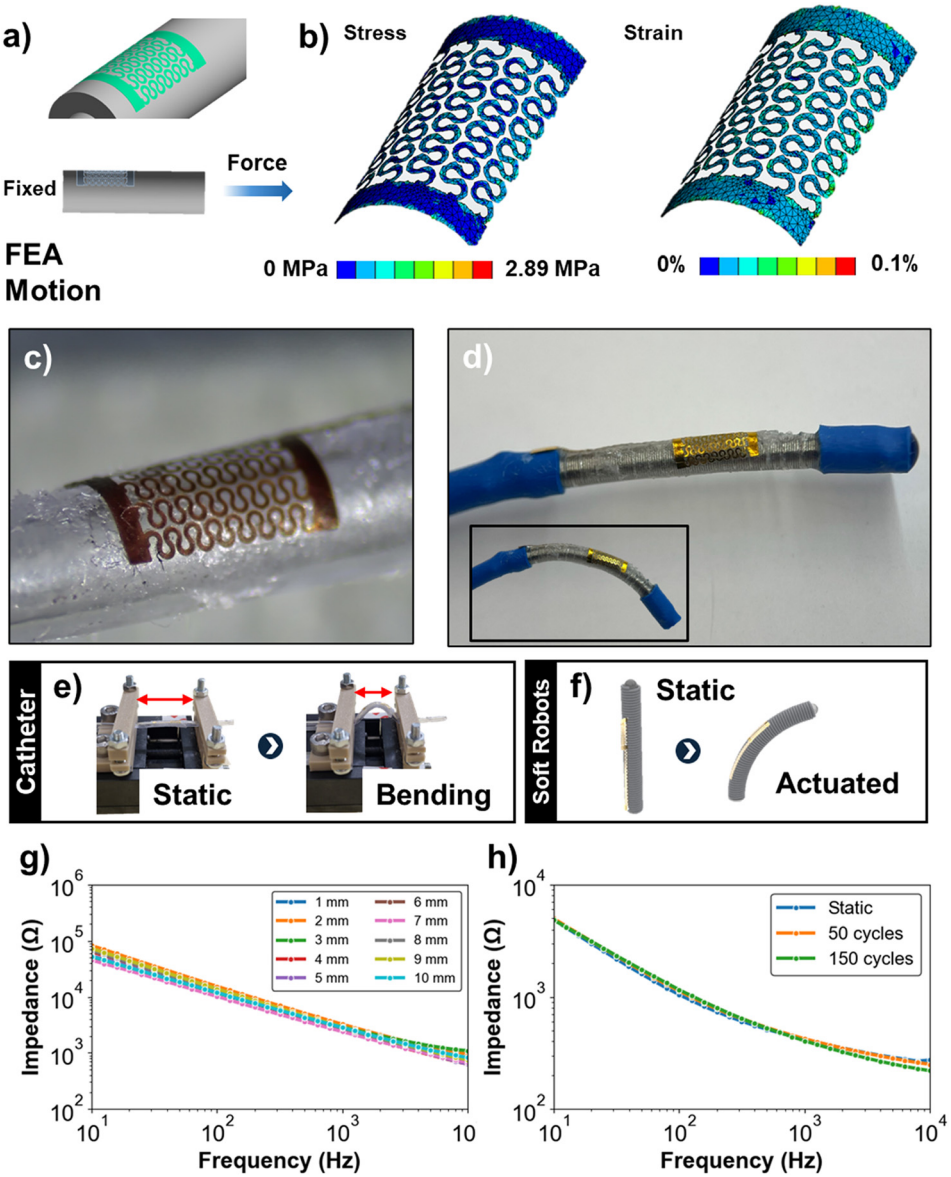

Fig. 3 (a) FEA model and uniaxial force applied in *a* direction for the computational study. (b) Stress and strain map of the flexible electrode as it is subjected to the uniaxial force. Integration of a flexible electrode to (c) a commercially available catheter and (d) a soft robot. (e) Mechanical stability test using a linear stage setup of the integrated catheter, showing the static and bending conditions during the test. (f) Visualisation of a soft robot's bending movement while integrated with the flexible electrode. The impedance results of the mechanical stability test after being subjected to different degrees of bending for the integrated catheter (g) and the number of cycles actuated on the integrated soft robot (h).

further validates the unchanging morphologies of mesoporous gold under repeated bending cycles. Although we can validate its stability during typical usage, long-term stability of the mechanical and electrochemical performance.

3.4. Integrated flexible electrode for EVD catheter

Leveraging the combined mechanical flexibility and superior electrochemical performance of mesoporous electrodes, we next evaluated their integration into extra ventricular drainage (EVD) catheters. EVD catheters are commonly used in neurosurgery to drain cerebrospinal fluid from patients with increased intracranial pressure.[4,49] The invasiveness of the device is a critical consideration as insertion can pose risks of hemorrhage, meningitis, and infection. Embedding sensors could potentially increase the device profile, heightening these risks, making it essential to assess the invasiveness of the integrated catheter. We employed a phantom brain model using a low concentration of agarose gel (0.6%), which exhibited similar mechanical properties to a human brain (Fig. 4a). After freehand insertion, the punctured areas were quantified using image processing. Multiple measurements were performed to account for variability, with mean values reported. As shown in Fig. 4b, the punch areas for plain catheters (5.71 mm^2) and those with integrated electrodes (5.85 mm^2) were nearly identical.

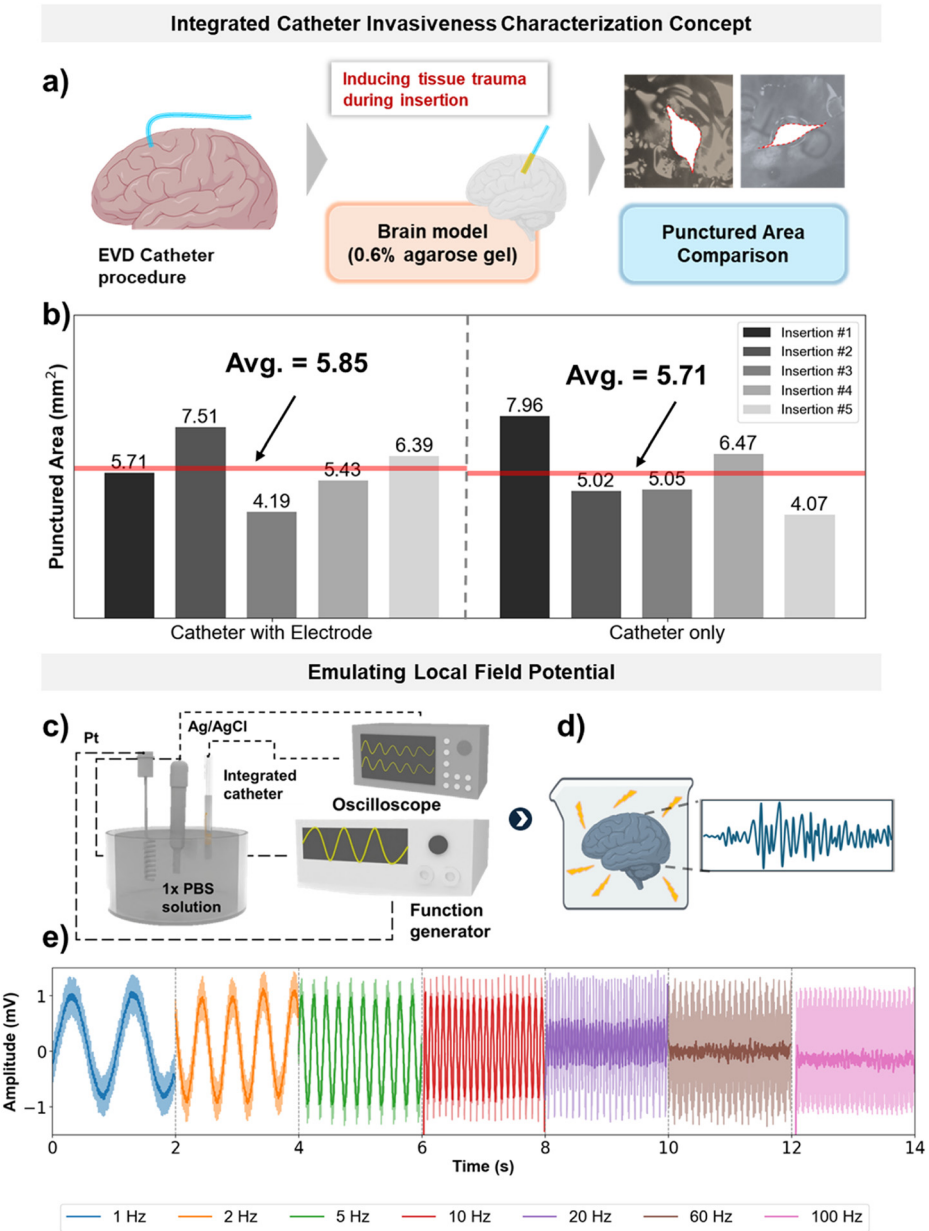

Fig. 4 Demonstration of mesoporous flexible electrode integration to EVD catheter. a) the concept of invasiveness characterization for the integrated catheter profile. b) the results of invasiveness characterization comparison between the plain catheter and the integrated catheter. c and d) Concept and experiment setup of the local field potential measurement functionality of the integrated catheter. e) The measurement of the integrated catheter on LFP signals generated through a function generator with various frequencies.

Statistical analysis showed that the 95% confidence interval (CI) indicates no substantial increase, and a two one-sided test (TOST) procedure using an equivalence margin of ±5 units confirmed that the integrated electrodes do not increase invasiveness. These results indicated that the thin, flexible mesoporous electrode maintains a low profile, suitable for safe integration into EVD catheters.

We further quantified the invasiveness of the system by measuring insertion forces using a universal testing machine (UTM) with the tips of both catheter types (with and without electrodes) attached to the load cell. The peak force associated with the first puncture was comparable across insertion speeds of 0.5 mm s^{-1}, 1 mm s^{-1}, and 1.5 mm s^{-1} (Fig. S13). Beyond this first peak, the integrated catheter exhibited a gradual increase in insertion force up to the maximum insertion depth (20 mm), whereas the plain catheter maintained a constant force. We attributed this difference to a slight mechanical mismatch and surface friction introduced by the flexible electrode, although localized tissue compaction may play a role.

The integrated, low impedance mesoporous electrode extends the functionality of EVD catheters by enabling signal recording during insertion. To demonstrate this capability, we utilized an *in vitro* benchtop setup in which sine wave

signals are generated by a constant electrical field (1 mVp-p and frequencies ranging from 1 Hz to 100 Hz) to a Pt counter electrode driven by a function generator (Fig. 4c). The integrated catheter and Pt electrode were then submerged in a 1× PBS solution to replicate physiological ionic conditions (Fig. 4d). Signals are recorded using an oscilloscope with a reference electrode (Ag/AgCl), and averaged signals recorded from the oscilloscope are then processed separately (Fig. 4e). This demonstration highlighted the capabilities of a flexible mesoporous electrode to capture electrical signals in the sub-millivolt range.

3.5. *Ex vivo* bioimpedance sensing demonstration

Conceptually, cells have extracellular resistance and intracellular/membrane resistance. Extracellular resistance reflects tissue composition and sodium levels of the extracellular fluids, while intracellular resistance comprises contributions from the biological system and the membrane (Fig. 5a). As these elements respond differently across different frequencies, impedance spectroscopy can provide insight into the intracellular conditions of a cell. Leveraging this principle, the integrated electrode enables characterization of tissue impedance and monitoring of ablation-induced changes. We apply thermal ablation to animal tissues using a commercially available electrocautery device (LED Surtron 120, StarkMed) and compare the change in impedance before and after ablation. The results show that the impedance increases in ablated tissue from 523 ± 7.4 Ω to 3.9 ± 1 kΩ at 1 kHz which is an increase of 86% (Fig. 5b). This overall impedance increase was due to the coagulation and charring that occurred in the tissue, consequently leading to the formation of insulating layers that increase its overall resistance. The increase spanned the entire measured frequency range (1 Hz–100 kHz), reflecting the loss of free water pathway for ion transport.

We observed a different phenomenon in plant tissues (potato tissue) used as a biological model system (Fig. 5c). Fresh slices exhibited higher impedance and a more capacitive phase response, indicative of intact cell membranes. Heating causes a significant decrease in the impedance from 8.43 ± 0.4 kΩ to 1.7 ± 0.07 kΩ at 1 kHz, which indicates the breakdown of the cell membrane, facilitating ion transfer. The phase angle also decreases significantly, showing a small capacitive resistance, implying the cell membrane breakdown. While in the lower frequency regions above 10 Hz, the resistance comparison between fresh slices and heated slices showed a slight difference, which was 14.8 ± 0.4 kΩ and 15.9 ± 0.6 kΩ, respectively. This difference in the lower frequency region was commonly caused by the electrode-electrolyte interaction. In this case, the slightly higher impedance value of the heated plant tissue can be attributed to the surface, reducing the medium for ion transfers. Additionally, we compared the impedance sensing of plant tissues between flat Au electrodes and mesoporous Au electrodes (Fig. S14). The overall trend shows notable differences as the impedance of heated tissue is

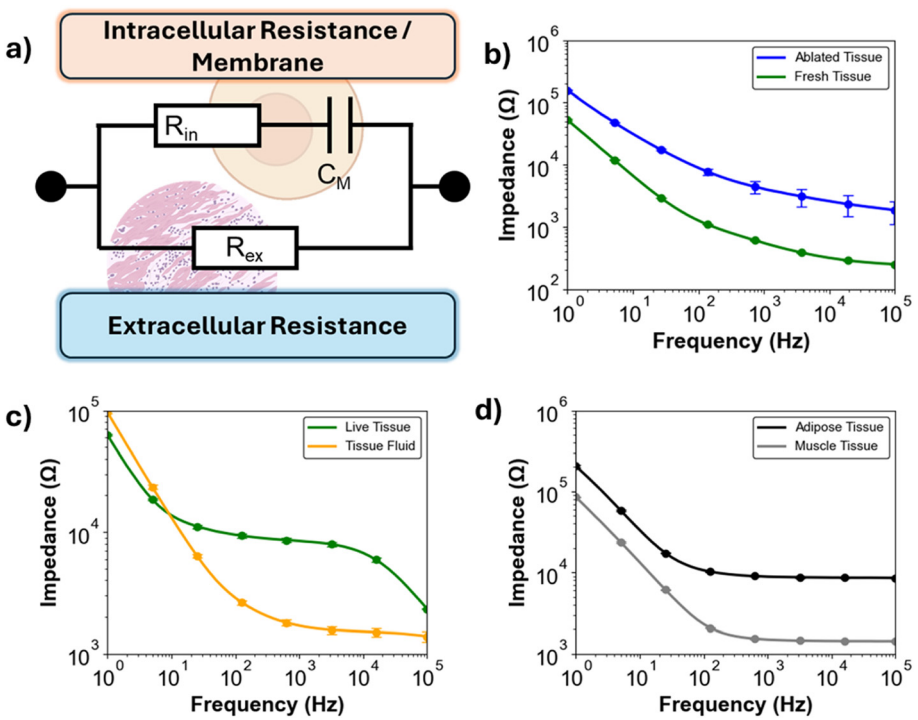

Fig. 5 (a) Bioimpedance sensing concept showing the extracellular resistance, intracellular resistance, and membrane capacitance as the main factors affecting bioimpedance analysis. (b) The impedance difference between ablated tissue and fresh tissue showcases post-ablation monitoring capability (c) impedance sensing of plant tissue (potato) comparison between live tissue and the fluid tissue after heating. (d) Impedance sensing comparison between adipose and muscle tissue.

overall higher for flat Au impedance sensing, as it has a higher impedance value compared to mesoporous Au electrodes. However, the heated potato impedance sensing also shows higher impedance across frequency regions, which indicates that the flat Au electrode impedance sensing is dominantly affected by the electrode-electrolyte interface rather than the potato tissue. The integrated electrode also distinguished tissue types such as adipose tissue and muscle tissue (Fig. 5d). The results show a higher impedance in adipose tissue than in muscle tissue due to their different composition. Adipose tissue has lower water content needed for ion transfer, which is reflected in a higher impedance across the frequency spectrum. Generally, from the standard deviation, impedance level variations increased as it entered the low frequency region, which is a common occurrence as low frequency impedances are more sensitive to noise and electrical drift. These demonstrations showcase the capability of flexible mesoporous electrodes to discriminate tissue conditions and compositions, which is relevant for intraoperative feedback and post-ablation monitoring.

3.6. *In vitro* cardiac organoid pacing

As well as EVD catheters, integrating electrodes onto a cardiac catheter enables cardio physiological mapping, pacing, and lesion removal, which have been widely adopted in clinical practice. To demonstrate this concept, we investigated the cardiac pacing functionality of our flexible mesoporous electrodes using human heart organoid models. We first characterized the charge injection capacity (CIC), a key parameter that defines the maximum safely deliverable charge before triggering irreversible electrochemical reactions. To quantify the water window, we conducted a CV scan of a gold electrode with a diameter of 500 μm in a 1× PBS solution from −2 V to 2 V. The cathodic water window of mesoporous gold is −1.4 V, comparable to that of flat gold (Fig. S15). The CIC parameter was obtained by applying biphasic stimulation under a typical 3-electrode setup in a 1× PBS solution, starting from 1000 μA to 3000 μA with a 1000 μs pulse width and 500 μs interphase gap. From the increasing stimulation series, we identified 2000 μA as the upper safe limit before the onset of irreversible reactions (Fig. S16). On the other hand, the flat gold counterpart displayed irreversible responses at a much lower stimulating current of 150 μA (Fig. S17). This showed that the mesoporous gold electrode has a capability to deliver larger stimulation amplitudes and a wider variety of pulse widths. From these limits, we can calculate the CIC of the mesoporous gold electrode, which is approximately 1019 μC cm^2, significantly higher than that of the flat gold electrode with an identical geometry, which is around 76 μC cm^2.

Upon CIC characterization, to validate our electrode's capability for cardiac pacing, we conducted an *in vitro* study using human cardiac organoids as a platform that can recapitulate heart function and spontaneous beating patterns. The organoid was cultured in a conical chamber where the flexible electrode was positioned at the base (Fig. 6c). Before transferring into the conical chamber, we observed the natural contraction of cardiac organoid using an optical microscope, showing the organoid intrinsic beating profile (Video S1). A digital camera was used to monitor the organoid contraction under electrical stimulation with a constant voltage and a varying frequency signal delivered through the porous electrode. The contraction frequencies were obtained by tracking the contour of organoid motion from video recordings (Video S2). Image analysis clearly indicates organoid contraction under applied 1 V square waves, with beating frequencies closely matching that of generated stimulation signals and beating capturing rate close to 100% as we detected 20 peaks out of 2 Hz electrical stimulation for 10 seconds (*e.g.*, ranging from 0.5 Hz to 2 Hz) (Fig. 6d). However, quantitatively, as we compared the detected peaks and electrical stimulation, there were slight timing differences in the organoid which aligns with common electrical stimulation caused by electromechanical delay of the organoid. As the frequency is higher, the timing differences decrease from 0.4 to 0.1 seconds approximately. This was due to our limitation on organoid beating observations using a camera that was detecting visible motion rather than electrical contraction, which becomes more noticeable on lower pacing frequencies. These results highlight the multimodality capability of our flexible electrodes, supporting both sensing and cardiac pacing functions.

4. Conclusion

In conclusion, this work reports the development of flexible mesoporous gold electrodes that can be seamlessly integrated into various MIS tools for on-site sensing and stimulation. The mesoporous layer provides 10-fold lower impedance and 6-fold higher charge storage than the typical flat Au electrodes. Our fabrication strategy, tailoring top-down laser machining and lithography together with bottom-up electrochemical deposition, is highly scalable and avoids manual compression steps used in prior studies, which offer limited enhancement in electrochemical performance. FEA and experimental validation confirm the mechanical flexibility and stretchability of the engineered porous electrode, which can accommodate multiple bending cycles of catheters and soft medical robotic systems. Unlike previous studies of sensors mounted onto passive catheters, our proposed solution of integrating thin film electrodes onto soft medical robots suggests an all-in-one system for both diagnosis and treatment in hard-to-reach anatomical regions. The mechanical compliance of serpentine-shaped mesoporous electrodes also allows for the integration into EVD/soft robots with a small diameter of 2 mm, retaining a low system profile, suitable for minimally invasive procedures. *In vitro* experiments with phantom samples, plant/animal tissues, together with human cardiac organoid

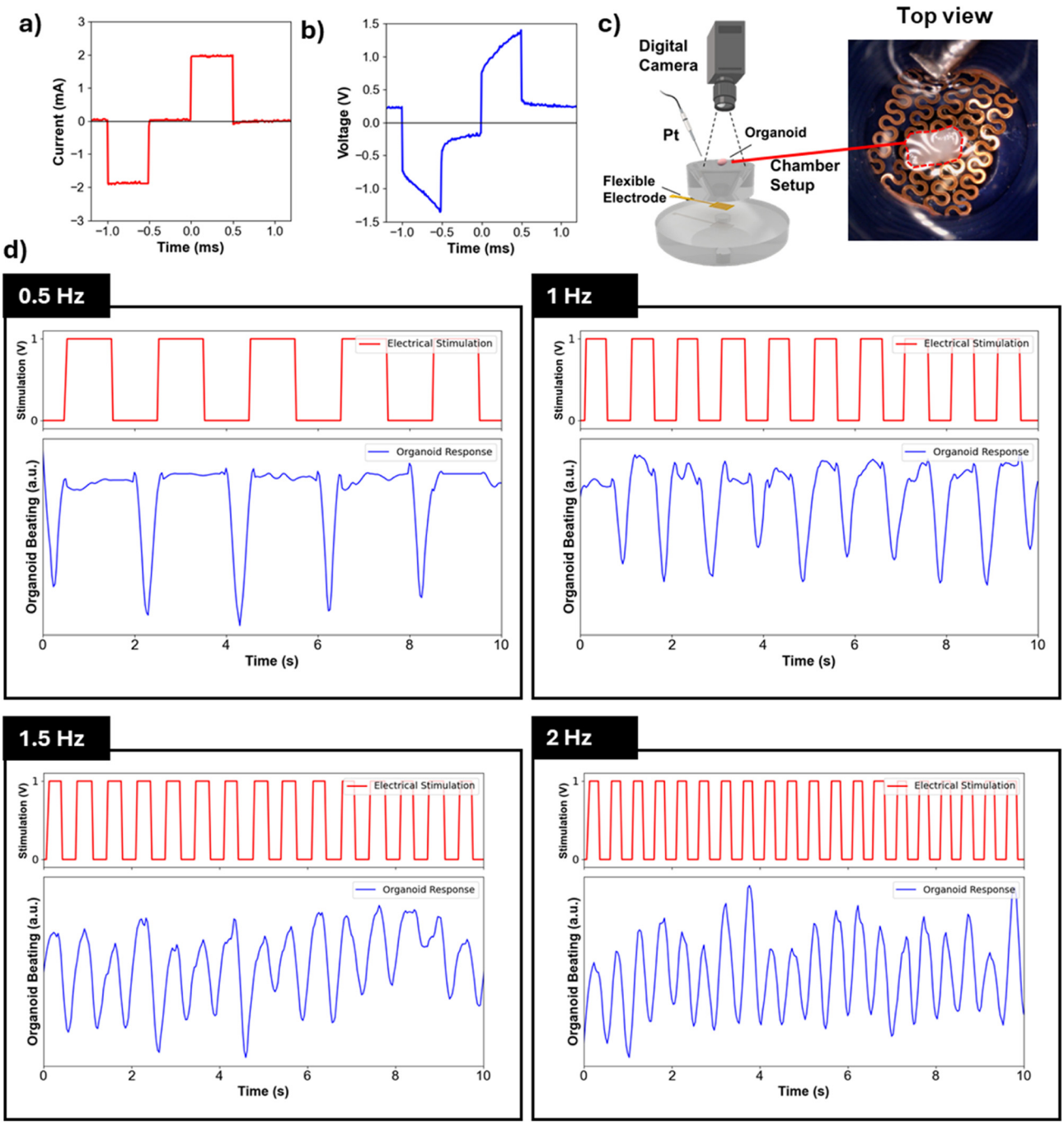

Fig. 6 Characterization of charge injection capacity (CIC) of the flexible mesoporous gold electrode (a) biphasic cathodic first stimulation limit that achieved the mesoporous gold electrode water window observed from the (b) voltage transient. (c) The experiment setup to administer electrical stimulation to human cardiac organoids while simultaneously monitoring their beating through a digital camera. (d) Synchronized organoid beating and electrical stimulation at various frequencies, starting from 0.5 Hz to 2 Hz.

modellings, demonstrate the versatility of these electrodes for impedance sensing and heart pacing. These results highlight the potential of mesoporous electrode-integrated MIS tools to improve the efficiency and functionality of catheterization procedures. Long term stability and its susceptibility to biofouling remain as the challenges of the device that can be explored in the future, especially for clinical applications of the device.

Author contributions

MAL and HPP conceptualized the study. MAL, CCN, NMD, and TBD designed and performed the experiments and analysed experimental data. MKM, ETC, JMC, and MNS provided the validation and characterization. MKM, ETC, JMC, MNS, CCN, HPP, NTD, YY reviewed the manuscript. QAN, YQ, and MAL visualized the experiments. MAL wrote

the original draft and revised version. HPP, JMC, ETC, and TND provided funding acquisition and resources.

Conflicts of interest

The authors declare that they have no competing interests.

Data availability

Essential data are provided in the main text and the supplementary information (SI). Data is available from the corresponding authors upon reasonable request.

Supplementary information is available. See https://doi.org/10.1039/d6lc00110f.

Acknowledgements

The authors acknowledge the support from the UNSW Scientia Fellowship Grant (PS46197 and PS77937), the Cancer Institute NSW Career Development Fellowship (PS66730), the UNSW GRIP Award (PS74064), Australian Research Council (DP240100961, FT240100203, and FL230100095), National Health and Medical Research Council (RG241515), the JST-ERATO (JPMJER2003), and Arto Hardy Family Biomedical Innovation Grant. This study was partly conducted at the Australian National Fabrication Facility, NSW Node, a firm founded under the National Collaborative Research Infrastructure Strategy to offer researchers in Australia with nano- and microfabrication capabilities.

References

1 M. Hepburn-Smith, I. Dynkevich, M. Spektor, A. Lord, B. Czeisler and A. Lewis, *J. Neurosci. Nurs.*, 2016, **48**, 54–65.
2 S. Hagel, T. Bruns, M. W. Pletz, C. Engel, R. Kalff and C. Ewald, *Interdiscip. Perspect. Infect. Dis.*, 2014, 708531.
3 J. Zhou, Y. Zhong, X. Li, H. Li, J. Wang, S. Yang and G. Chen, *Neurology: Clinical Practice*, 2023, **13**, e200156.
4 P. Y. M. Woo, B. C. F. Ng, J. X. Xiao, D. Wong, A. Seto, S. Lam, C. Yim, H. Y. Lo, Y. C. Po, L. Y. W. Wong, M. W. Y. Lee, K. Y. Yam, J. K. S. Pu, K. Y. Chan and W. S. Poon, *Acta Neurochir.*, 2019, **161**, 1623–1632.
5 M. Xu, Z. Song, W. Hong, L. Wang, C. Jiang, B. Yang, M. Qin and J. Liu, *Adv. Funct. Mater.*, 2023, **33**, 2302041.
6 R. H. Dean, R. L. McCann and L. B. Schwartz, *J. Vasc. Surg.*, 1991, **14**, a30062.
7 A. S. Manolis, P. J. Wang and N. A. M. Estes, *Radiofrequency Catheter Ablation for Cardiac Tachyarrhythmias*, 1994.
8 F. H. M. Wittkampf, R. van Es and K. Neven, *JACC: Clinical Electrophysiology*, 2018, **8**, 977–986.
9 Y. S. Choi, R. T. Yin, A. Pfenniger, J. Koo, R. Avila, K. Benjamin Lee, S. W. Chen, G. Lee, G. Li, Y. Qiao, A. Murillo-Berlioz, A. Kiss, S. Han, S. M. Lee, C. Li, Z. Xie, Y. Y. Chen, A. Burrell, B. Geist, H. Jeong, J. Kim, H. J. Yoon, A. Banks, S. K. Kang, Z. J. Zhang, C. R. Haney, A. V. Sahakian, D. Johnson, T. Efimova, Y. Huang, G. D. Trachiotis, B. P. Knight, R. K. Arora, I. R. Efimov and J. A. Rogers, *Nat. Biotechnol.*, 2021, **39**, 1228–1238.
10 C. C. Nguyen, T. Teh, M. T. Thai, P. T. Phan, T. T. Hoang, H. Low, J. Davies, E. Nicotra, N. H. Lovell and T. N. Do, in *Proceedings - IEEE International Conference on Robotics and Automation*, Institute of Electrical and Electronics Engineers Inc., 2022, pp. 9579–9585.
11 F. Holmqvist, M. Kesek, A. Englund, C. Blomström-Lundqvist, L. O. Karlsson, G. Kennebäck, D. Poçi, R. Samo-Ayou, R. Sigurjónsdóttir, M. Ringborn, C. Herczku, J. Carlson, E. Fengsrud, F. Tabrizi, N. Höglund, S. Lönnerholm, O. Kongstad, A. Jönsson and P. Insulander, *Eur. Heart J.*, 2019, **40**, 820–830.
12 M. Han, L. Chen, K. Aras, C. Liang, X. Chen, H. Zhao, K. Li, N. R. Faye, B. Sun, J. H. Kim, W. Bai, Q. Yang, Y. Ma, W. Lu, E. Song, J. M. Baek, Y. Lee, C. Liu, J. B. Model, G. Yang, R. Ghaffari, Y. Huang, I. R. Efimov and J. A. Rogers, *Nat. Biomed. Eng.*, 2020, **4**, 997–1009.
13 Y. Li, D. Li, J. Wang, T. Ye, Q. Li, L. Li, R. Gao, Y. Wang, J. Ren, F. Li, J. Lu, E. He, Y. Jiao, L. Wang and Y. Zhang, *Adv. Funct. Mater.*, 2023, **34**, 2310260.
14 C. Li, P. M. Wu, Z. Wu, C. H. Ahn, D. Ledoux, L. A. Shutter, J. A. Hartings and R. K. Narayan, *Biomed. Microdevices*, 2012, **14**, 109–118.
15 G. Rozen, L. Ptaszek, I. Zilberman, K. Cordaro, E. K. Heist, C. Beeckler, A. Altmann, Z. Ying, Z. Liu, J. N. Ruskin, A. Govari and M. Mansour, *Heart Rhythm*, 2017, **14**, 248–254.
16 B. Gil, B. Li, A. Gao and G. Z. Yang, *ACS Appl. Electron. Mater.*, 2020, **2**, 2669–2677.
17 K. V. Meena and A. Ravi Sankar, *IEEE Sens. J.*, 2021, **21**, 10241–10290.
18 B. Gil, B. Lo, G. Z. Yang and S. Anastasova, *Mater. Today Bio*, 2022, **15**, 100298.
19 B. A. Taha, I. A. Al-Tahar, A. J. Addie, A. B. Mahdi, A. J. Haider, Y. Al Mashhadany, V. Chaudhary and N. Arsad, *Appl. Mater. Today*, 2024, **38**, 102229.
20 H. Yi, H. Kim, K. R. Kim, J. H. Kim, J. Kim, H. Lee, S. S. Grewal, W. D. Freeman and W. H. Yeo, *Biosens. Bioelectron.*, 2024, **255**, 116267.
21 Z. Chen, Z. Lin, S. N. Obaid, E. Rytkin, S. A. George, C. Bach, M. Madrid, M. Liu, J. LaPiano, A. Fehr, X. Shi, N. Quirion, B. Russo, H. Knight, A. Aduwari, I. R. Efimov and L. Lu, *Sci. Adv.*, 2023, **9**, eadi0757.
22 A. F. Renz, J. Lee, K. Tybrandt, M. Brzezinski, D. A. Lorenzo, M. Cerra Cheraka, J. Lee, F. Helmchen, J. Vörös and C. M. Lewis, *Adv. Healthcare Mater.*, 2020, **9**, 2000814.
23 M. Asplund, *Science Robotics*, 2023, **8**, 78.
24 J. Li, Y. B. Seng, G. Ponraj, K. S. Kumar, C. J. Cai and H. Ren, in *2021 IEEE 17th International Conference on Wearable and Implantable Body Sensor Networks, BSN 2021*, Institute of Electrical and Electronics Engineers Inc., 2021.
25 W. Yang, A. Broski, J. Wu, Q. H. Fan and W. Li, *IEEE Trans. Nanotechnol.*, 2018, **17**, 701–704.
26 W. Yang, Y. Gong, C. Y. Yao, M. Shrestha, Y. Jia, Z. Qiu, Q. H. Fan, A. Weber and W. Li, *Lab Chip*, 2021, **21**, 1096–1108.
27 S. R. Dupont, F. Novoa, E. Voroshazi and R. H. Dauskardt, *Adv. Funct. Mater.*, 2014, **24**, 1325–1332.

28 K. Xie, A. Glasser, S. Shinde, Z. Zhang, J. M. Rampnoux, A. Maali, E. Cloutet, G. Hadziioannou and H. Kellay, *Adv. Funct. Mater.*, 2021, **31**, 2009039.
29 Y. Lu, T. Wang, Z. Cai, Y. Cao, H. Yang and Y. Y. Duan, *Sens. Actuators, B*, 2009, **137**, 334–339.
30 R. Kim and Y. Nam, *J. Neural Eng.*, 2015, **12**(2), DOI: 10.1088/1741-2560/12/2/026010.
31 C. Li, Z. Wu, K. Limnuson, C. Cheyuo, P. Wang, C. H. Ahn, R. K. Narayan and J. A. Hartings, *Biomed. Microdevices*, 2016, **18**, 1–10.
32 R. Pomfret, G. Miranpuri and K. Sillay, *Ann. Neurosci.*, 2013, **20**(3), 118–22.
33 E. Tomaskovic-Crook, Q. Gu, S. N. A. Rahim, G. G. Wallace and J. M. Crook, *Cell*, 2020, **9**, 658.
34 E. Tomaskovic-Crook, S. L. Higginbottom, B. Zhang, J. Bourke, G. G. Wallace and J. M. Crook, *Organoids*, 2023, **2**, 20–36.
35 Y. Zhang, S. Wang, X. Li, J. A. Fan, S. Xu, Y. M. Song, K. J. Choi, W. H. Yeo, W. Lee, S. N. Nazaar, B. Lu, L. Yin, K. C. Hwang, J. A. Rogers and Y. Huang, *Adv. Funct. Mater.*, 2014, **24**, 2028–2037.
36 A. J. Bandodkar, J. Choi, S. P. Lee, W. J. Jeang, P. Agyare, P. Gutruf, S. Wang, R. A. Sponenburg, J. T. Reeder, S. Schon, T. R. Ray, S. Chen, S. Mehta, S. Ruiz and J. A. Rogers, *Adv. Mater.*, 2019, **31**, 1902109.
37 C. C. Nguyen, J. Davies, A. Ashok, T. T. Hoang, A. Ehteda, T. B. Dang, E. Nicotra, H. A. Tran, B. Sharma, K. Zhu, P. T. Phan, A. Ji, J. Wan, J. Rnjak-Kovacina, O. Vittorio, H. P. Phan, N. H. Lovell and T. N. Do, *Adv. Healthcare Mater.*, 2025, **14**, 2404623.
38 C. Li, Ö. Dag, T. D. Dao, T. Nagao, Y. Sakamoto, T. Kimura, O. Terasaki and Y. Yamauchi, *Nat. Commun.*, 2015, **6**, 6608.
39 E. Ahmed, M. K. Masud, P. Komatineni, S. Dey, R. Lobb, M. S. A. Hossain, A. Möller, Y. Yamauchi, A. A. I. Sina and M. Trau, *Biosens. Bioelectron.*, 2024, **249**, 115984.
40 Y. Qiu, A. Ashok, C. C. Nguyen, E. Tomaskovic-Crook, M. A. Listyawan, T. A. Truong, K. Zhu, H. Chen, M. N. Shivdasani, T. N. Do, Y. Yamauchi, J. M. Crook and H. P. Phan, *ACS Appl. Mater. Interfaces*, 2025, **17**, 48440–48452.
41 K. B. Shanmugasundaram, E. Ahmed, X. Miao, A. Kulasinghe, J. A. Fletcher, J. Monkman, P. Mainwaring, M. K. Masud, H. Park, M. S. A. Hossain, Y. Yamauchi, A. A. I. Sina, K. O'Byrne, A. Wuethrich and M. Trau, *ACS Sens.*, 2024, **9**, 3009–3016.
42 H. Park, M. K. Masud, A. Ashok, M. Kim, M. A. Wahab, J. Zhou, Y. Terasawa, C. S. Gallo, N. T. Nguyen, M. S. A. Hossain, Y. Yamauchi and Y. V. Kaneti, *Small*, 2024, **20**, 2311645.
43 A. Hua, Z. Mai, B. Wu, Z. Ji, M. Fu, Y. Hu and S. Huang, *Mater. Today Phys.*, 2022, **26**, 100728.
44 S. P. Lee, L. E. Klinker, L. Ptaszek, J. Work, C. Liu, F. Quivara, C. Webb, C. Dagdeviren, J. A. Wright, J. N. Ruskin, M. Slepian, Y. Huang, M. Mansour, J. A. Rogers and R. Ghaffari, *Proc. IEEE*, 2015, **103**, 682–689.
45 W. N. Sharpe, J. Pulskamp, C. Eberl, D. S. Gianola and K. J. Hemker, *TENSILE STRESS-STRAIN CURVES OF GOLD FILM*, 2006.
46 S. T. Chen, in *Materials Research Society Symposium - Proceedings*, Materials Research Society, 1995, vol. 381, pp. 141–146.
47 J. Kirkup, *The history and evolution of surgical instruments Vil Catheters, hollow needles and other tubular instruments*, 1998, vol. 80.
48 T. D. Long, D. F. Kallmes, R. Hanel, T. Shigematsu, A. M. Halaszyn, J. Wolter and A. Berenstein, *J. NeuroInterventional Surg.*, 2019, **11**, 179–183.
49 M. Hepburn-Smith, I. Dynkevich, M. Spektor, A. Lord, B. Czeisler and A. Lewis, *J. Neurosci. Nurs.*, 2016, **48**, 54–65.